JℲM PAPERS

Actuation manifold from snapshot data

Luigi Marra[1,†], **Guy Y. Cornejo Maceda**[2], **Andrea Meilán-Vila**[3],
Vanesa Guerrero[3], **Salma Rashwan**[1], **Bernd R. Noack**[2,4,†], **Stefano Discetti**[1]
and Andrea Ianiro[1]

[1]Department of Aerospace Engineering, Universidad Carlos III de Madrid, Av. de la Universidad, 30, Leganés, 28911 Madrid, Spain

[2]Chair of Artificial Intelligence and Aerodynamics, School of Mechanical Engineering and Automation, Harbin Institute of Technology, 518055 Shenzhen, PR China

[3]Department of Statistics, Universidad Carlos III de Madrid, Calle Madrid, 126, Getafe, 28903 Madrid, Spain

[4]Guangdong Provincial Key Laboratory of Intelligent Morphing Mechanisms and Adaptive Robotics, Harbin Institute of Technology, 518055 Shenzhen, PR China

We propose a data-driven methodology to learn a low-dimensional manifold of controlled flows. The starting point is resolving snapshot flow data for a representative ensemble of actuations. Key enablers for the actuation manifold are isometric mapping as encoder, and a combination of a neural network and a *k*-nearest-neighbour interpolation as decoder. This methodology is tested for the fluidic pinball, a cluster of three parallel cylinders perpendicular to the oncoming uniform flow. The centres of these cylinders are the vertices of an equilateral triangle pointing upstream. The flow is manipulated by constant rotation of the cylinders, i.e. described by three actuation parameters. The Reynolds number based on a cylinder diameter is chosen to be 30. The unforced flow yields statistically symmetric periodic shedding represented by a one-dimensional limit cycle. The proposed methodology yields a five-dimensional manifold describing a wide range of dynamics with small representation error. Interestingly, the manifold coordinates automatically unveil physically meaningful parameters. Two of them describe the downstream periodic vortex shedding. The other three describe the near-field actuation, i.e. the strength of boat-tailing, the Magnus effect and forward stagnation point. The manifold is shown to be a key enabler for control-oriented flow estimation.

Key words: low-dimensional models, machine learning

† Email addresses for correspondence: luigi.marra@uc3m.es, bernd.noack@hit.edu.cn

1. Introduction

In this study, we propose a data-driven manifold learner of the flows for a large range of operating conditions demonstrated by a low-dimensional manifold for the actuated fluidic pinball. A cornerstone of theoretical fluid mechanics is the low-dimensional representation of coherent structures. This representation is a basis for understanding dynamic modelling, sensor-based flow estimation, model-based control and optimisation.

Many avenues of reduced-order representations have been proposed. Leonardo da Vinci presented coherent structures and vortices artfully as sketches in a time when the Navier–Stokes equations were not known (Marusic & Broomhall 2021). A quantitative pathway of low-dimensional modelling was started by Hermann von Helmholtz (1858) with his vortex laws. Highlights are the von Kármán (1912) model of the vortex street and derivation of feedback wake stabilisation from the Föppl's vortex model by Protas (2004). Orr and Sommerfeld added a stability framework culminating in Stuart's mean-field theory (Stuart 1958) to incorporate non-linear Reynolds stress effects. The proper orthogonal decomposition (POD) has quickly become the major data-driven approach to compress snapshot data into a low-dimensional Galerkin expansion (Berkooz, Holmes & Lumley 1993). Cluster-based modelling is an alternative data-driven flow compression, coarse-graining snapshot data into a small set of representative centroids (Kaiser *et al.* 2014). All these low-dimensional flow representations are the kinematic prelude to dynamic models, e.g. point vortex models, modal stability approaches (Theofilis 2011), POD Galerkin models (Holmes *et al.* 2012) and cluster-based network models (Fernex, Noack & Semaan 2021).

Data-driven manifold learners are a recent highly promising avenue of reduced-order representations. A two-dimensional manifold may, for instance, accurately resolve transient cylinder wakes: the manifold dimension is a tiny fraction of the number of vortices, POD modes and clusters required for a similar resolution. This manifold may be obtained by mean-field considerations (Noack *et al.* 2003), by dynamic features (Loiseau, Noack & Brunton 2018), by locally linear embedding (Noack *et al.* 2023) and by isometric mapping (ISOMAP, Farzamnik *et al.* 2023). In all these approaches, the manifolds have been determined for a single operating condition. Haller *et al.* (2023) emphasised a key challenge, namely, it remains 'unclear if these manifolds are robust under parameter changes or under the addition of external, time-dependent forcing'. In this study, we thus aim to identify a manifold representing fluid flows for a rich set of control actions by incorporating the actuation commands.

We choose the fluidic pinball as our benchmark problem for the proposed manifold learning. This configuration has been proposed by Ishar *et al.* (2019) as a geometrically simple two-dimensional configuration with a rich dynamic complexity under cylinder actuation and Reynolds number change. The transition scenario is described and modelled by Deng *et al.* (2020) comprising a sequence of bifurcations before passing to chaotic behaviour. The feedback stabilisation achieved through cylinder rotation has been accomplished with many different approaches (Raibaudo *et al.* 2020; Cornejo Maceda *et al.* 2021; Li *et al.* 2022; Wang *et al.* 2023). Farzamnik *et al.* (2023) have demonstrated that the unforced dynamics can be described on a low-dimensional manifold.

In this study, we illustrate the development of the control-oriented manifold, called an 'actuation manifold' in the following, for the fluidic pinball with three steady cylinder rotations as independent inputs. ISOMAP is chosen for its superior compression capability and manifold interpretability over other techniques such as POD (Farzamnik *et al.* 2023).

The rest of the article is structured as follows. In § 2 we introduce the dataset of the actuated fluidic pinball while in § 3 we discuss the methodology employed to distill the

actuation manifold and to use it for flow-estimation purposes. The results are presented and discussed in § 4, before highlighting the main conclusions of the work in § 5.

2. Flow control dataset

The dataset is based on two-dimensional incompressible uniform flow past three cylinders of equal diameter D. Their vertices form an equilateral triangle with one vertex pointing upstream and its median aligned with the streamwise direction. The origin of the Cartesian reference system is located in the midpoint between the two rightmost cylinders. The streamwise and crosswise directions are indicated with x and y, respectively. The corresponding velocity components are indicated with u and v. The computational domain Ω is bounded in $[-6, 20] \times [-6, 6]$, and the unstructured grid used has 4225 triangles and 8633 nodes. The snapshots are linearly interpolated on a structured grid with a spacing of 0.05 in both x and y directions to maintain a format similar to the experimental data and for greater simplicity.

The Reynolds number (Re), which is based on D and the incoming velocity U_∞, is set to 30 for all cases. A reference time scale D/U_∞ is set as a convective unit (c.u.). The force coefficients C_L and C_D are obtained by normalising respectively lift and the drag forces with $\frac{1}{2}\rho U_\infty^2 D$, being ρ the density of the fluid.

The control is achieved with independent cylinder rotations included in the vector $\boldsymbol{b} = (b_1, b_2, b_3)^{\mathrm{T}}$, where b_1, b_2 and b_3 refer to the tangential speeds of the front, top and bottom cylinder, respectively. Here, 'T' denotes the transpose operator. Positive actuation values correspond to counter-clockwise rotations. Combinations of rotational speed ranging from -3 to 3 by steps of 1 (i.e. $-3, -2, \ldots, 3$) have been used, for a total of 343 configurations, including the unforced case. Each of these simulation is run for 800 c.u. to reach the steady state and snapshots with 1 c.u. separation in the last 20 c.u. for each steady state have been sampled. This time is chosen to approximately cover two shedding cycles of the unforced case. This dataset therefore consists of 20 post-transient snapshots for each of the 343 combinations of actuations explored, for a total of $M = 6860$ snapshots.

The actuations are condensed into a three-parameter vector, denoted as $\boldsymbol{p} = (p_1, p_2, p_3)^{\mathrm{T}}$, and referred to as Kiki parameters (Lin 2021). These three parameters describe the three mechanisms of boat-tailing ($p_1 = (b_3 - b_2)/2$), Magnus effect ($p_2 = b_1 + b_2 + b_3$) and forward stagnation point control ($p_3 = b_1$). The Kiki parameters are introduced for an easier physical interpretation of the actuation commands.

3. Methodology

A n-dimensional manifold is a topological space in which every point has a neighbourhood homeomorphic to Euclidean space $\mathbb{R}^n$. The approach proposed here involves employing an encoder–decoder strategy to acquire actuation manifolds, incorporating ISOMAP (Tenenbaum, de Silva & Langford 2000), neural networks and k-nearest-neighbour (kNN) algorithms (Fix & Hodges 1989). The collected dataset undergoes ISOMAP to discern a low-dimensional embedding. Then, the flow reconstruction procedure involves mapping actuation and sensor information to the manifold coordinates, followed by interpolation among the kNNs to estimate the corresponding snapshot. An overview of this procedure is illustrated in figure 1 and detailed in the following.

If we consider our flow fields as vector functions $\boldsymbol{u}(\boldsymbol{x}) = (u(x, y), v(x, y))$ belonging to a Hilbert space, the inner product between two snapshots $\boldsymbol{u}_i$ and $\boldsymbol{u}_j$
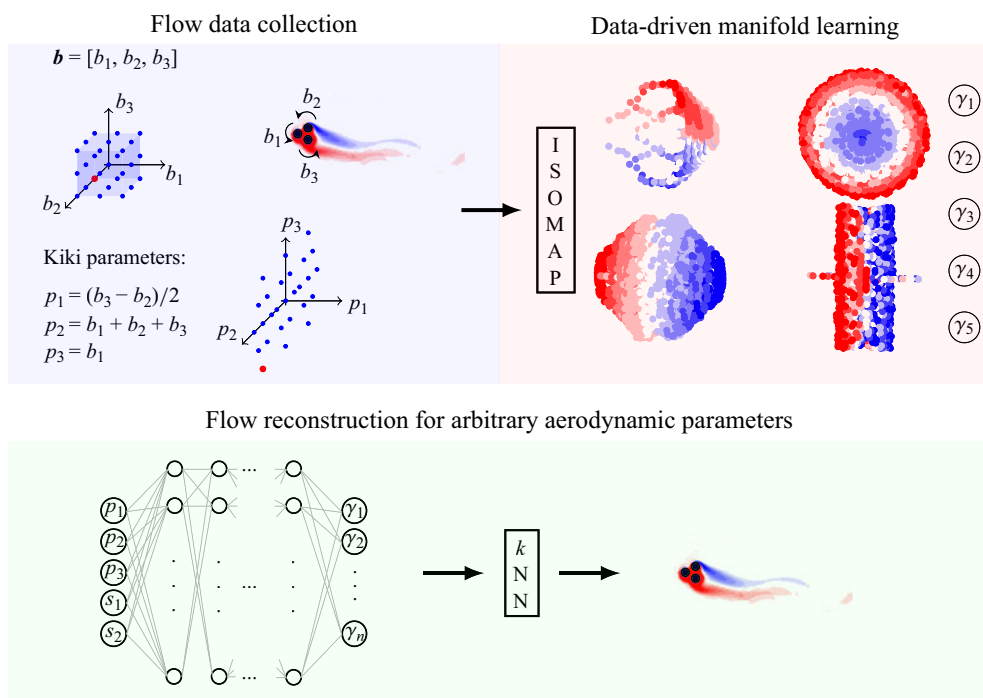
Figure 1. Illustration of the methodology for actuation-manifold learning and full-state estimation. The diagram highlights key steps, from flow data collection to data-driven actuation manifold discovery (upper section). A neural network, incorporating actuation parameters (p_1, p_2 and p_3) and sensor information (s_1 and s_2), determines ISOMAP coordinates ($\gamma_1, \gamma_2, \ldots, \gamma_n$) and a kNN decoder is used for the full-state flow reconstruction.

is defined by

$$\langle \boldsymbol{u}_i, \boldsymbol{u}_j \rangle = \iint_{\Omega} \boldsymbol{u}_i(x, y) \cdot \boldsymbol{u}_j(x, y) \, \mathrm{d}x \, \mathrm{d}y, \tag{3.1}$$

where '$\cdot$' refers to the scalar product in the two-dimensional vector space. Norms are canonically defined by $\|\boldsymbol{u}\| = \sqrt{\langle \boldsymbol{u}, \boldsymbol{u} \rangle}$ and distances between snapshots are consistent with this norm.

For our study, we have a collection of M flow field snapshots. In the encoder procedure, the ISOMAP algorithm necessitates determining the square matrix $\boldsymbol{D}_{\mathrm{G}} \in \mathbb{R}^{M \times M}$ containing the geodesic distances among snapshots. Geodesic distances are approximated by selecting a set of neighbours for each snapshot to create a kNN graph. Within these neighbourhoods, snapshots are linked by paths whose lengths correspond to Hilbert-space distances. Geodesic distances between non-neighbours are then obtained as the shortest path through neighbouring snapshots in the kNN graph (Floyd 1962). At this stage, selecting the number of neighbours, which in the encoding part we denote by k_e, is crucial for creating the kNN graph and thus approximating the geodesic distance matrix.

Existing techniques are mostly empirical as in Samko, Marshall & Rosin (2006). The method proposed by Samko *et al.* (2006) was successfully used by Farzamnik *et al.* (2023). However, due to the particularity of our dataset, as explained later in the article, standard empirical methods did not yield acceptable results. For this reason, we use the approach based on the Frobenius norm (denoted by $\| \cdot \|_F$) of the geodesic distance matrix $\boldsymbol{D}_{\mathrm{G}}$ (Shao & Huang 2005) to determine k_e. Opting for a small k_e can lead to disconnected regions and

undefined distances within the dataset. Thus, there exists a minimum value of k_e ensuring that all snapshots are linked in the kNN graph. Starting from this minimum, increasing k_e results in more connections in the kNN graph, causing the Frobenius norm of the geodesic distance matrix to decrease monotonically. However, using an excessively large value may cause a short-circuiting within the kNN graph. Eventually, this yields an Euclidean representation, thus losing ISOMAP's capability to unfold nonlinear relationships within the dataset. Such short-circuiting is indicated by a sudden drop in $\|\boldsymbol{D}_G\|_F$ with increasing k_e. Thus, the minimum and the value at which short-circuiting first occurs define a suitable range of k_e to be selected to approximate the geodesic distance matrix. The choice of k_e within this range is generally based on how well the high-dimensional data are represented in the low-dimensional space. This is measured in terms of residual variance, as done by Kouropteva, Okun & Pietikäinen (2002).

After constructing the geodesic distance matrix $\boldsymbol{D}_G$, multidimensional scaling (Torgerson 1952) is employed to construct the low-dimensional embedding $\boldsymbol{\Gamma} = (\tilde{\gamma}_{ij})_{1 \leqslant i \leqslant M, \, 1 \leqslant j \leqslant n}$, whose dimension is n. The jth column of the matrix $\boldsymbol{\Gamma}$ is the jth ISOMAP coordinate for all the M flow field snapshots. We refer to the ISOMAP coordinates with $\gamma_j, j = 1, \ldots, n$. Consequently, $\tilde{\gamma}_{ij} = \gamma_j(i), i = 1, \ldots, M$.

More specifically, to obtain the low-dimensional embedding, we need to minimise the cost function:

$$\|\boldsymbol{\Gamma}\boldsymbol{\Gamma}^T - \boldsymbol{B}\|_F^2, \tag{3.2}$$

where $\boldsymbol{B}$ is the double-centred squared-geodesic distance matrix $\boldsymbol{B} = -1/2\boldsymbol{H}^T(\boldsymbol{D}_G \odot \boldsymbol{D}_G)\boldsymbol{H}$. The centring matrix $\boldsymbol{H}$ is defined as $\boldsymbol{H} = \boldsymbol{I}_M - (1/M)\boldsymbol{1}_M$. Here $\boldsymbol{I}_M$ and $\boldsymbol{1}_M$ are the identity matrix and the matrix with all unit components of size $M \times M$, respectively. The symbol $\odot$ refers to the Hadamard product. The solution of the minimisation term in (3.2) involves the eigenvalues and eigenvectors arising from the decomposition of $\boldsymbol{B}$, specifically $\boldsymbol{B} = \boldsymbol{V}\boldsymbol{\Lambda}\boldsymbol{V}^T$. For a given n, we select the n largest positive eigenvalues, i.e. $\boldsymbol{\Lambda}_n$, and the corresponding eigenvectors $\boldsymbol{V}_n$. The coordinates are obtained by scaling these eigenvectors by the square roots of their corresponding eigenvalues. Thus, the coordinates are given by $\boldsymbol{\Gamma} = \boldsymbol{V}_n\boldsymbol{\Lambda}_n^{1/2}$, where $\boldsymbol{\Lambda}_n^{1/2}$ is a diagonal matrix containing the square roots of the n largest eigenvalues.

In this instance, following the methodology outlined by Tenenbaum *et al.* (2000), the evaluation of data representation quality within the ISOMAP technique is conducted through the residual variance $R_v = 1 - R^2(\text{vec}(\boldsymbol{D}_G), \text{vec}(\boldsymbol{D}_E))$. Here $R^2(\cdot, \cdot)$ denotes the squared correlation coefficient, 'vec' is the vectorisation operator and $\boldsymbol{D}_E$ represents the matrix of the Euclidean distances between the low-dimensional representation of all the snapshots, retaining only the first n ISOMAP coordinates. The residual variance indicates the ability of the low-dimensional embedding to reproduce the geodesic distances in the high-dimensional space. The dimension n of the low-dimensional embedding is typically determined by identifying an elbow in the residual variance plot.

After the actuation manifold identification, the objective is to perform a flow reconstruction from the knowledge of a reduced number of sensors and actuation parameters. This process is carried out in two steps. First, a regression model is trained to identify the low-dimensional representation of a snapshot. Specifically, we employ a fully connected multi-layer perceptron (MLP) to map the actuation parameters and sensor information to the ISOMAP coordinates. It is possible to employ as network input either the actuation or the Kiki parameters. In the following, we employ the Kiki parameters since we deem them more elegant, although this does not substantially affect the results, being the Kiki parameters a linear combination of the actuation parameters. Second, a decoding procedure is conducted through linear interpolation among a fixed number (denoted by

k_d) of nearest neighbours, following the methodology established by Farzamnik *et al.* (2023). An alternative to this mapping is presented in Appendix A, where a two-step kNN regression with distance-weighted averaging is employed. It is important to clarify that the decoding step is applicable only for interpolation cases, meaning for actuation cases that fall within the limits explored during the dataset generation, i.e. $|b_i| < 3$, $\forall i = 1, 2, 3$, with $|\cdot|$ being the absolute value.

4. Results

4.1. *Identification and physical interpretation of the low-dimensional embedding*

The results of the encoding step are represented in figure 2. First, the neighbourhood size k_e for the encoding must be determined. The Frobenius norm of the geodesic distance matrix $||\boldsymbol{D}_G||_F$ as a function of k_e is reported in figure 2(*a*). A minimum $k_e = 40$ is required to ensure that all the neighbourhoods are connected. Figure 2(*b*) reports the percentage of connected snapshots in the kNN graph. This percentage reaches 100 % for $k_e = 40$. Below this value, the manifold is divided into disjointed regions. By increasing k_e starting from the minimum value, the Frobenius norm decreases due to improved connections between neighbourhoods. This also raises the probability of short-circuits, which drastically reduces $||\boldsymbol{D}_G||_F$. Indeed, the first short-circuiting is identified for $k_e = 60$. Choosing a value of k_e within the range from the minimum value up to the point where the first significant drop in $||\boldsymbol{D}_G||_F$ occurs does not result in substantial alterations of the geometry of the manifold or the physical interpretation of its coordinates. Therefore, in this paper, we select the minimum value, that is $k_e = 40$.

Then the residual variance is used to search for the true dimensionality of the dataset. Employing $n = 5$ coordinates leads to a residual variance of less than 10 %, thus $n = 5$ dimensions are deemed sufficient to describe the manifold, as shown in figure 2(*c*). Further increase in the number of dimensions provides only marginal changes in the residual variance.

The representation of the five-dimensional embedding is undertaken in figure 2(*d*) in the form of two-dimensional projections on the $\gamma_i - \gamma_j$ planes with $i, j = 1, \ldots, 5$ and $i < j$. A first visual observation of the projections highlights interesting physical interpretations. The projection on the $\gamma_3 - \gamma_4$ plane unveils a circular shape, suggesting that these two coordinates describe a periodic feature, i.e. the vortex shedding in the wake of the pinball. The fact that the circle is full suggests that different control actions result in an enhanced or attenuated vortex shedding. Each steady state describes a circle in the $\gamma_3 - \gamma_4$ plane. The radius of each circle explains the amplitude of vortex shedding, while the angular position provides information about the phase. Cases that do not exhibit vortex shedding collapse into points where $\gamma_3, \gamma_4 \approx 0$. This is evident from the observation of the projections on the planes $\gamma_1 - \gamma_3$ and $\gamma_1 - \gamma_4$, both returning a champagne coupe shape, suggesting that smaller values of γ_1 are a prerogative of the cases with limit cycle of smaller amplitude.

This feature also suggests that γ_1 is correlated with the boat tailing parameter p_1 and thus with the drag coefficient C_D, as visualised in figure 3. This plot also shows a correlation between γ_2, the Magnus parameter p_2 and the lift coefficient C_L. The fifth coordinate of the low-dimensional embedding γ_5, on the other hand, appears to be correlated with the stagnation point parameter p_3 and partially explains the lift produced by the pinball. Intriguingly, all ISOMAP coordinates are physically meaningful and allow us to discover the three Kiki parameters without human input.

Another interesting physical interpretation arises observing the manifold section $\gamma_1 - \gamma_2$, as shown in figure 4. This provides insights into the horizontal symmetry of
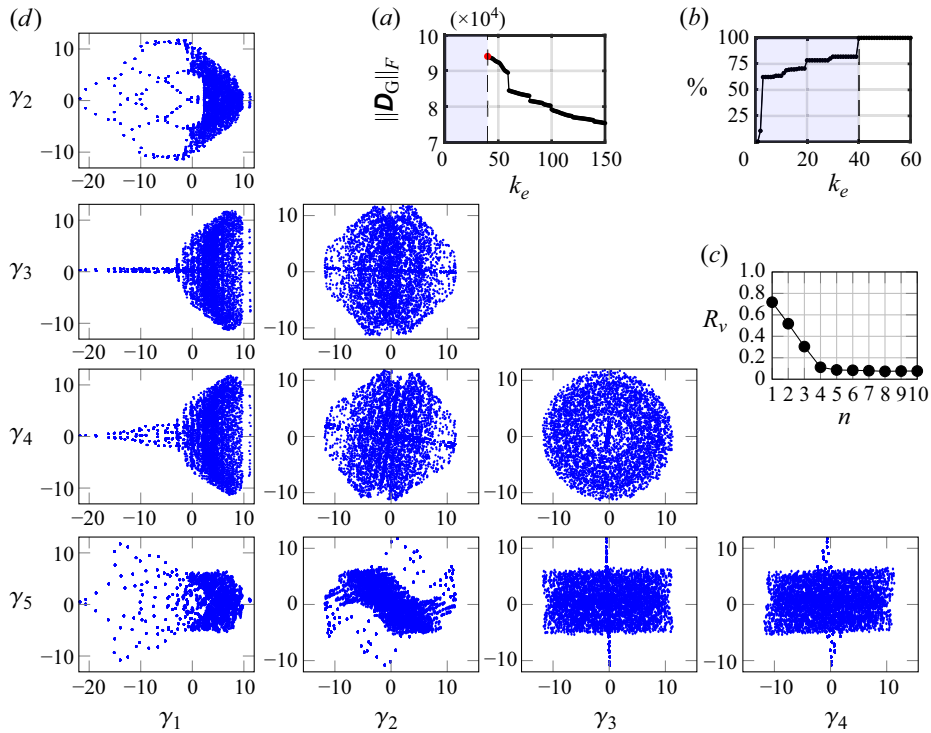
Figure 2. (*a*) The Frobenius norm of the geodesic distance matrix plotted against the number of neighbours employed in Floyd's algorithm. (*b*) The ratio between the connected snapshots and the total number of snapshots as k_e increases. Results of the manifold obtained for $k_e = 40$ are presented in panels (*c,d*). The former illustrates the residual variance of the first 10 ISOMAP coordinates, whereas the latter showcases all possible manifold sections identified by the first five coordinates.

the data. In the figure, semicircles repeat, increasing in number as γ_1 increases. Within each of them, b_1 varies from -3 to 3, whereas b_2 and b_3 remain fixed. The branches symmetrically positioned with respect to the axis $\gamma_2 = 0$ are associated with symmetric actuation b_2 and b_3.

The low-dimensional embedding, being the result of the eigenvector decomposition of the double-centred squared-geodesic distance matrix, is made of orthogonal vectors. While this might represent a disadvantage to autoencoders (Otto & Rowley 2022), this also allows projecting the snapshots on this basis and obtaining spatial modes that can be used to corroborate the physical interpretation of the manifold coordinates. The jth spatial mode $\boldsymbol{\phi}_j$, $j = 1, \ldots, n$ is a linear combination of the snapshots $\boldsymbol{u}_i$, i.e. $(\sum_{i=1}^{M} \gamma_{ij}^2)^{1/2}\boldsymbol{\phi}_j = \sum_{i=1}^{M} \tilde{\gamma}_{ij}\boldsymbol{u}_i$.

The first five ISOMAP modes are visualised in figure 5 with a line integral convolution (LIC; Forssell & Cohen 1995) plot superimposed on a velocity magnitude contour plot. The visual observation of the modes confirms the interpretation of the physical meaning of the coordinates of the low-dimensional embedding. Three modes, namely $\boldsymbol{\phi}_1, \boldsymbol{\phi}_2$ and $\boldsymbol{\phi}_5$ are representative of the actuation parameters. The first ISOMAP mode is characterised by the presence of a jet (wake) downstream of the pinball due to boat-tailing (base bleeding). The second ISOMAP mode represents a circulating motion around the pinball, responsible for positive or negative lift, depending on the circulation direction. The fifth mode is
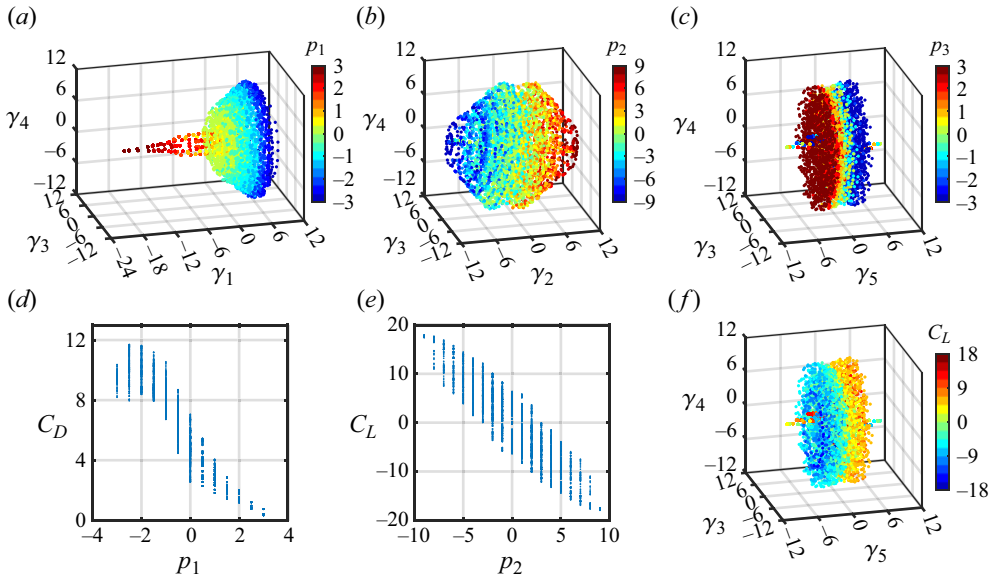
Figure 3. Three-dimensional projections of the manifold colour-coded with actuation parameters and forces coefficients. The first (boat-tailing) and second (Magnus) actuation parameters are plotted against lift and drag coefficients to understand physical control mechanisms.

characterised by a net circulation around the front cylinder, determining the position of the front cylinder stagnation point, if added to the mean field. The two spatial modes ϕ_3 and ϕ_4, instead, have the classical aspect of vortex shedding modes. Together, they describe the wake response to actuation parameters (far field), providing information on the intensity and phase of vortex shedding.

4.2. *Flow estimation*

For the identification of the low-dimensional representation of a snapshot, we employ a fully connected MLP. The mapping is done having as inputs the Kiki parameters and two sensors. The mapping also includes sensor information because each actuation vector is associated with a limit cycle, which in our case is described by 20 post-transient snapshots. Therefore, the actuation vector provides comprehensive knowledge of the coordinates representing the near field (γ_1, γ_2 and γ_5). Far-field coordinates (γ_3 and γ_4) identification requires information about the phase of vortex shedding, which is provided by the sensors. Two different alternatives are proposed here. In the first, we utilise the lift coefficient and its one-quarter mean shedding period delay (we refer to this case with MLP$_1$). In the second, crosswise components of velocity are measured at two positions in the wake, specifically at points $x_1 = (7, 1.25)$ and $x_2 = (10, 1.25)$ (MLP$_2$). The sensors are located in the crosswise position at the edge of the shear layer of the unforced case, i.e. at the top of the upper cylinder. The streamwise location is selected such that the vortex shedding is already developed. The streamwise separation between the two sensors is such that the flight time between them is approximately one-quarter of the shedding period in the unforced case. This ensures that the sensor data collect relevant information for the flow reconstruction, even though a systematic position optimisation has not been performed. The characteristics of the employed networks are summarised in table 1. The training of the neural networks is performed with the dataset used to construct the data-driven
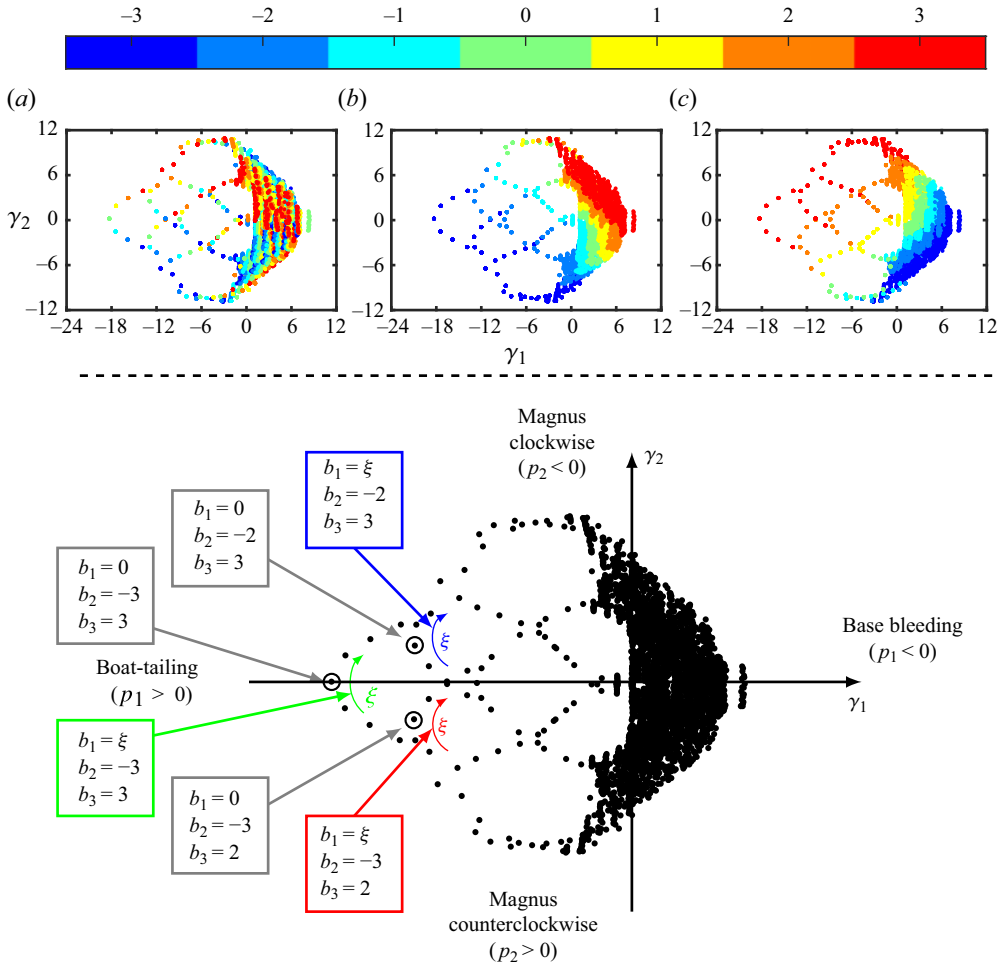
996 A26-8

Figure 4. At the top, representation of the manifold section identified by the coordinates γ_1 and γ_2 colour coded with b_1 (*a*), b_2 (*b*) and b_3 (*c*). At the bottom, a diagram explaining how the coordinate γ_2 provides indications of horizontal symmetry in the flow field.
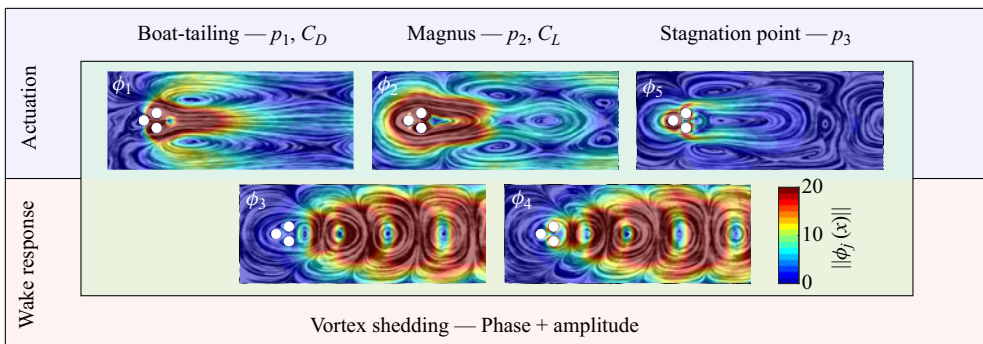

Figure 5. LIC representations of the normalised actuation modes. The shadowed contour represents the local velocity magnitude of the pseudomodes.

Input layer size	5	Output layer size	5
Number of samples	6860	Loss	Mean square error
Training set	80 %	Batch size	2048
Validation set	20 %	Number of epochs	Early stop on validation loss
Test set	22 external cases	Optimiser	Adam
I/O scaling	Mean − std → [0, 1]	Activation function	tanh
Hidden layers MLP$_1$	(70, 70, 70, 70)	Hidden layers MLP$_2$	(40, 40)

Table 1. Structure of the neural networks used for latent coordinate identification.

manifold randomly removing all snapshots related to 20 % of the actuation cases and using the remaining snapshots for validation.

To test the accuracy of flow estimation, we use 22 additional simulations with randomly selected actuation, not present in the training nor the validation dataset. As done for the training dataset, the last 20 c.u. are sampled every 1 c.u. for a total of 440 snapshots. The neural networks are used to identify the low-dimensional representation of the snapshots in the test dataset and then the kNN decoder is applied to reconstruct the full state. In the decoding phase, we select $k_d = 220$.

The value of k_d was chosen by performing a parametric study. In particular, we selected the k_d to minimise the reconstruction error of the snapshots in the validation dataset. The selected k_d is considerably higher than the k_e. A reason for this result lies in the particular topology of the present dataset. For some specific control actions, vortex shedding is completely suppressed, resulting in a stationary post-transient solution. The cases with no shedding have 20 snapshots sampled in the post-transient identical to each other. Likewise, their representation in low-dimensional space is identical. When decoding using the kNN interpolation, for snapshots close to those without shedding, considering a low k_d is equivalent to considering a small number of directions for the estimation of the gradients, which is not sufficient and results in a reconstruction with considerable error. To get a practical idea, considering $k_d < 20$ would be equivalent to considering only one direction, which is insufficient for decoding. Such a dataset topology greatly complicates the choice of k_d, suggesting the need to identify a k_d that is locally optimal. Such a choice, however, goes beyond the scope of the present research and is deferred to future work.

The accuracy of the estimation between the true (u_i) and estimated ($\hat{u}_i$) snapshots is quantified in terms of cosine similarity $S_G(u_i, \hat{u}_i) = \langle u_i, \hat{u}_i \rangle / (\|u_i\| \|\hat{u}_i\|)$. Results can be observed in figure 6, the knowledge of the manifold enables a full state estimation with few sensors and minimal reconstruction error. When performing the flow reconstruction using MLP$_1$, the median cosine similarity is 0.9977, corresponding to a median root-mean-square error (RMSE) of 0.0512. Using MLP$_2$, instead, the median cosine similarity is 0.9990 (RMSE = 0.0336).

5. Conclusions

In this study, we have addressed a challenge of reduced-order modelling: accurate low-dimensional representations for a large range of operating conditions. The flow data are compressed in a manifold using ISOMAP as encoder and kNN as decoder. The methodology is demonstrated for the fluidic pinball as an established benchmark problem of modelling and control. The cylinder rotations are used as three independent steady control parameters. The starting point of the reduced-order modelling is a dataset with
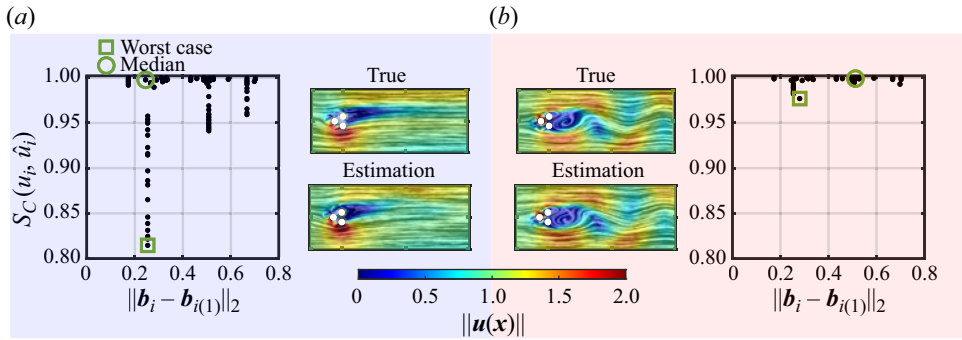
Figure 6. Cosine similarity between real and reconstructed snapshots for all 22 actuation cases in the test dataset. Reconstruction error is plotted against the distance of each actuation case (b_i) to its nearest neighbour in the training dataset $b_{i(1)}$. In the centre, a comparison between the true snapshot and its estimation is presented for the median error case. Figure presented with LIC and color-coded by velocity magnitude. The number of neighbours is fixed to $k_d = 220$. Results are shown for MLP_1 (*a*) and MLP_2 (*b*).

20 statistically representative post-transient snapshots at $Re = 30$ for 343 sets of cylinder rotations covering uniformly a box with circumferential velocities between -3 and 3.

The ISOMAP manifold describes all snapshots with 5 latent variables and few per cent representation errors. To the best of the authors' knowledge, this is the first demonstration of data-driven manifold learning for a flow under multiple input control. Intriguingly, all latent variables are aligned with clear physical meanings. Three coordinates correspond to near-field actuation effects. More precisely, these coordinates are strongly aligned with the Kiki parameters p introduced by Lin (2021), describing (i) the level of boat-tailing (base bleeding) p_1 leading to drag reduction (increase), (ii) the strength of the Magnus effect p_2 leading to a steady lift and characterising (iii) the forward stagnation point p_3. Two further coordinates correspond to the wake response to actuation, i.e. the amplitude and phase of vortex shedding. The distillation of physically meaningful parameters from a fully automated manifold is surprising and inspiring (see figure 1).

Our low-rank model is a key enabler for flow estimation with a minimum number of sensors. It is possible to estimate the full flow state with small reconstruction errors just by knowing the actuation parameters and employing two additional measurements, namely the aerodynamic forces or the flow velocity in two points of the wake.

We emphasise that the low-dimensional characterisation of post-transient dynamics as a function of three actuations constitutes a modelling challenge and encourages numerous further applications, e.g. vortex-induced vibration of a cylinder at different spring stiffnesses and cylinder masses, aerodynamic flutter of an elastic airfoil with different wing elasticities, combustion instabilities for different reaction parameters, just to name a few. A low-dimensional manifold representation can be utilised for understanding, estimation, prediction and model-based control. In summary, the presented results can be expected to inspire a large range of applications and complementary manifold learning methods.

996 A26-11

Declaration of interests. The authors report no conflict of interest.

Author ORCIDs.

- Luigi Marra https://orcid.org/0000-0001-9422-2808;
- Guy Y. Cornejo Maceda https://orcid.org/0000-0001-7499-7569;
- Andrea Meilán-Vila https://orcid.org/0000-0001-8537-9280;
- Vanesa Guerrero https://orcid.org/0000-0002-6610-7455;
- Salma Rashwan https://orcid.org/0000-0003-4618-3765;
- Bernd R. Noack https://orcid.org/0000-0001-5935-1962;
- Stefano Discetti https://orcid.org/0000-0001-9025-1505;
- Andrea Ianiro https://orcid.org/0000-0001-7342-4814.

Appendix A. Comparison between neural network and kNN performances in the decoding step

In this appendix, we propose an alternative to the decoding as illustrated in figure 1. In this approach, the decoding is carried out only utilising a kNN regression with weighted averaging with the inverse of distances between neighbours. We transition from actuation parameters and sensor data to the low-dimensional representation of a snapshot using an initial kNN regression, with a number of neighbours indicated as k_{d_1}. Subsequently, we move from the manifold coordinates to the full state reconstruction using another kNN regression, with a number of neighbours indicated as k_{d_2}.

Consider the estimation of a snapshot $\boldsymbol{u}_i$ based on the actuation vector and sensor information in the vector $\boldsymbol{z}_i = (p_1, p_2, p_3, s_1, s_2)^{\mathrm{T}}$. We estimate the low-dimensional representation of this snapshot, which we denoted as $\hat{\boldsymbol{y}}_i$, utilising the first kNN regression. Therefore, starting from $\boldsymbol{z}_i$, we consider its k_{d_1}-nearest vectors in the dataset, denoted as $\boldsymbol{z}_{i(1)}, \ldots, \boldsymbol{z}_{i(k_{d_1})}$, and their counterparts in the low-dimensional embedding $\boldsymbol{y}_{i(1)}, \ldots, \boldsymbol{y}_{i(k_{d_1})}$ to derive $\hat{\boldsymbol{y}}_i$ as follows:

$$\hat{\boldsymbol{y}}_i = \frac{\sum_{j=1}^{k_{d_1}} \boldsymbol{y}_{i(j)} ||\boldsymbol{z}_{i(j)} - \boldsymbol{z}_i||^{-1}}{\sum_{j=1}^{k_{d_1}} ||\boldsymbol{z}_{i(j)} - \boldsymbol{z}_i||^{-1}}. \tag{A1}$$

Subsequently, the same procedure is applied to estimate the snapshot, denoted as $\hat{\boldsymbol{u}}_i$. We consider the k_{d_2} nearest vectors to $\hat{\boldsymbol{y}}_i$, labelled as $\hat{\boldsymbol{y}}_{i(1)}, \ldots, \hat{\boldsymbol{y}}_{i(k_{d_2})}$, and their counterparts
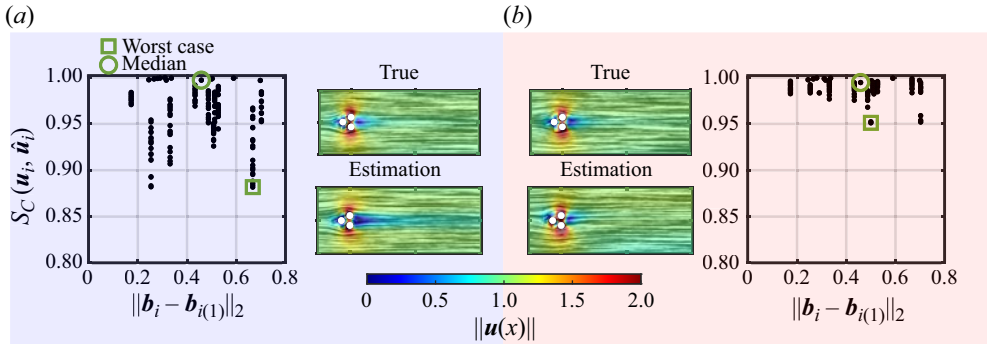
Figure 7. Cosine similarity between real and reconstructed snapshots for all 22 actuation cases in the test dataset. Reconstruction error is plotted against the distance of each actuation case to its nearest neighbour in the training dataset. In the centre, a comparison between the true snapshot and its estimation is presented for the median error case. Figure presented with LIC and color-coded by velocity magnitude. Results are shown force for sensors (*a*) and velocity sensors (*b*).

	kNN + kNN regression				MLP + kNN interpolation	
	k_{d_1}	k_{d_2}	Median S_C	Median RMSE	Median S_C	Median RMSE
Sensing forces	69	7	0.9970	0.0573	0.9977	0.0512
Sensing velocities	66	7	0.9946	0.0804	0.9990	0.0336

Table 2. Comparison of reconstruction errors in terms of cosine similarity and RMSE for both sensing cases using the two decoding methodologies: two-step kNN regression (left) and neural network and kNN interpolation (right). The table also includes the values of k_{d_1} and k_{d_2} used in the two-step kNN regression decoding method.

in the high-dimensional space $\boldsymbol{u}_{i(1)}, \ldots, \boldsymbol{u}_{i(k_{d_2})}$ to obtain the estimate as follows:

$$\hat{\boldsymbol{u}}_i = \frac{\sum_{j=1}^{k_{d_2}} \boldsymbol{u}_{i(j)} ||\hat{\boldsymbol{y}}_{i(j)} - \hat{\boldsymbol{y}}_i||^{-1}}{\sum_{j=1}^{k_{d_2}} ||\hat{\boldsymbol{y}}_{i(j)} - \hat{\boldsymbol{y}}_i||^{-1}}. \tag{A2}$$

For the selection of k_{d_1} and k_{d_2} we have to solve the minimisation problems in (A3):

$$\begin{cases} \operatorname*{argmin}_{k_{d_1}} \sum_{i=1}^{M} \left(\hat{\boldsymbol{y}}_i^{(-m),k_{d_1}} - \boldsymbol{y}_i \right)^2, \\ \operatorname*{argmin}_{k_{d_2}} \sum_{i=1}^{M} \left(\hat{\boldsymbol{u}}_i^{(-m),k_{d_2}} - \boldsymbol{u}_i \right)^2, \end{cases} \tag{A3}$$

where $\hat{\boldsymbol{y}}_i^{(-m),k_{d_1}}$ and $\hat{\boldsymbol{u}}_i^{(-m),k_{d_2}}$ are the estimations of $\boldsymbol{y}_i$ and $\boldsymbol{u}_i$ using the kNN regression with k_{d_1} and k_{d_2} neighbours, respectively, and using as the training dataset all snapshots except the $m = 20$ snapshots of the limit cycle to which the ith snapshot, being estimated, belongs. The procedure follow the same principles of the leave-one-out cross-validation (Wand & Jones 1994), but instead of eliminating only one case for the estimation, all snapshots of the limit cycle corresponding to the execution are eliminated. The results of

the snapshot reconstruction using k NN regression in the two steps of the decoding process are presented in figure 7.

Table 2 lists the values of k_{d_1} and k_{d_2} used for reconstructing the snapshots in the testing dataset for both sensing cases. In addition, the table also includes the reconstruction errors in terms of median cosine similarity and RMSE. The reconstruction performance is only slightly worse if compared with the case where a neural network followed by kNN interpolation is used.

REFERENCES

BERKOOZ, G., HOLMES, P. & LUMLEY, J.L. 1993 The proper orthogonal decomposition in the analysis of turbulent flows. *Annu. Rev. Fluid Mech.* **25** (1), 539–575.

CORNEJO MACEDA, G.Y., LI, Y., LUSSEYRAN, F., MORZYŃSKI, M. & NOACK, B.R. 2021 Stabilization of the fluidic pinball with gradient-enriched machine learning control. *J. Fluid Mech.* **917**, A42.

DENG, N., NOACK, B.R., MORZYŃSKI, M. & PASTUR, L.R. 2020 Low-order model for successive bifurcations of the fluidic pinball. *J. Fluid Mech.* **884**, A37.

FARZAMNIK, E., IANIRO, A., DISCETTI, S., DENG, N., OBERLEITHNER, K., NOACK, B.R. & GUERRERO, V. 2023 From snapshots to manifolds – a tale of shear flows. *J. Fluid Mech.* **955**, A34.

FERNEX, D., NOACK, B.R. & SEMAAN, R. 2021 Cluster-based network modeling—from snapshots to complex dynamical systems. *Sci. Adv.* **7** (25), eabf5006.

FIX, E. & HODGES, J.L. 1989 Discriminatory analysis. Nonparametric discrimination: consistency properties. *Intl Stat. Rev.* **57** (3), 238–247.

FLOYD, R.W. 1962 Algorithm 97: shortest path. *Commun. ACM* **5** (6), 345.

FORSSELL, L.K. & COHEN, S.D. 1995 Using line integral convolution for flow visualization: curvilinear grids, variable-speed animation, and unsteady flows. *IEEE Trans. Vis. Comput. Graphics* **1** (2), 133–141.

HALLER, G., KASZÁS, B., LIU, A. & AXÅS, J. 2023 Nonlinear model reduction to fractional and mixed-mode spectral submanifolds. *Chaos* **33** (6), 063138.

HELMHOLTZ, H. 1858 Über integrale der hydrodynamischen gleichungen, welche den wirbelbewegungen entsprechen. *J. Reine Angew. Math.* **55**, 25–55.

HOLMES, P., LUMLEY, J.L., BERKOOZ, G. & ROWLEY, C.W. 2012 *Turbulence, Coherent Structures, Dynamical Systems and Symmetry*. Cambridge University Press.

ISHAR, R., KAISER, E., MORZYŃSKI, M., FERNEX, D., SEMAAN, R., ALBERS, M., MEYSONNAT, P.S., SCHRÖDER, W. & NOACK, B.R. 2019 Metric for attractor overlap. *J. Fluid Mech.* **874**, 720–755.

KAISER, E., NOACK, B.R., CORDIER, L., SPOHN, A., SEGOND, M., ABEL, M., DAVILLER, G., ÖSTH, J., KRAJNOVIĆ, S. & NIVEN, R.K. 2014 Cluster-based reduced-order modelling of a mixing layer. *J. Fluid Mech.* **754**, 365–414.

VON KÁRMÁN, T. 1912 Über den Mechanismus des Wiederstandes, den ein bewegter Körper in einer Flüssigkeit erfahrt. *Nachr. Ges. Wiss. Göttingen* **1912**, 547–556.

KOUROPTEVA, O., OKUN, O. & PIETIKÄINEN, M. 2002 Selection of the optimal parameter value for the locally linear embedding algorithm. In *FSDK'02, Proceedings of the 1st International Conference on Fuzzy Systems and Knowledge Discovery: Computational Intelligence for the E-Age, Singapore* (ed. L. Wang, S. K. Halgamuge & X. Yao). pp. 359–363.

LI, Y., CUI, W., JIA, Q., LI, Q., YANG, Z., MORZYŃSKI, M. & NOACK, B.R. 2022 Explorative gradient method for active drag reduction of the fluidic pinball and slanted Ahmed body. *J. Fluid Mech.* **932**, A7.

LIN, Q. 2021 Fully automated control-oriented reduced-order modeling exemplified for the fluidic pinball. Master's thesis, Harbin Institute of Technology.

LOISEAU, J.-CH., NOACK, B.R. & BRUNTON, S.L. 2018 Sparse reduced-order modeling: sensor-based dynamics to full-state estimation. *J. Fluid Mech.* **844**, 459–490.

MARUSIC, I. & BROOMHALL, S. 2021 Leonardo da Vinci and fluid mechanics. *Annu. Rev. Fluid Mech.* **53**, 1–25.

NOACK, B.R., AFANASIEV, K., MORZYŃSKI, M., TADMOR, G. & THIELE, F. 2003 A hierarchy of low-dimensional models for the transient and post-transient cylinder wake. *J. Fluid Mech.* **497**, 335–363.

NOACK, B.R., EHLERT, A., NAYERI, C.N. & MORZYNSKI, M. 2023 Analysis, modeling, and control of the cylinder wake. In *Data-Driven Fluid Mechanics: Combining First Principles and Machine Learning* (ed. M.A. Mendez, A. Ianiro, B.R. Noack & S.L. Brunton), pp. 3–19. Cambridge University Press.

OTTO, S.E. & ROWLEY, C.W. 2022 Inadequacy of linear methods for minimal sensor placement and feature selection in nonlinear systems: a new approach using secants. *J. Nonlinear Sci.* **32** (5), 69.

PROTAS, B. 2004 Linear feedback stabilization of laminar vortex shedding based on a point vortex model. *Phys. Fluids* **16** (12), 4473–4488.

RAIBAUDO, C., ZHONG, P., NOACK, B.R. & MARTINUZZI, R.J. 2020 Machine learning strategies applied to the control of a fluidic pinball. *Phys. Fluids* **32**, 015108.

SAMKO, O., MARSHALL, A.D. & ROSIN, P.L. 2006 Selection of the optimal parameter value for the isomap algorithm. *Pattern Recognit. Lett.* **27** (9), 968–979.

SHAO, C. & HUANG, H. 2005 Selection of the optimal parameter value for the isomap algorithm. In *MICAI 2005: Advances in Artificial Intelligence* (ed. A. Gelbukh, Á. de Albornoz & H. Terashima-Marín), pp. 396–404. Springer.

STUART, J.T. 1958 On the non-linear mechanics of hydrodynamic stability. *J. Fluid Mech.* **4** (1), 1–21.

TENENBAUM, J.B., DE SILVA, V. & LANGFORD, J.C. 2000 A global geometric framework for nonlinear dimensionality reduction. *Science* **290** (5500), 2319–2323.

THEOFILIS, V. 2011 Global linear instability. *Annu. Rev. Fluid Mech.* **43**, 319–352.

TORGERSON, W.S. 1952 Multidimensional scaling: I. Theory and method. *Psychometrika* **17** (4), 401–419.

WAND, M.P. & JONES, M.C. 1994 *Kernel Smoothing*. Chapman & Hall/CRC Monographs on Statistics & Applied Probability, vol. 60. Chapman & Hall.

WANG, X., DENG, N., CORNEJO MACEDA, G.Y. & NOACK, B.R. 2023 Cluster-based control for net drag reduction of the fluidic pinball. *Phys. Fluids* **35** (2), 023601.